Comparison of Staggered Grid Finite Difference Schemes for Ultrasound Simulation in Curving Composites

Erik Frankforter[1, a)], Cara Leckey[1], and William Schneck III[1]

[1]*Nasa Langley Research Center, Hampton, VA 23681, United States*

[a)]Corresponding author: erik.frankforter@nasa.gov

Abstract. The optimization of ultrasonic nondestructive evaluation (NDE) simulation tools for composites has the potential to reduce both individual part inspection time and overall certification time for composite parts and structures. Inspection guidance based on simulation provides increased confidence in the veracity of inspection results in addition to time reductions. This paper outlines ongoing work targeted to advance this objective through the use of finite difference (FD) simulation techniques formulated for composite structures with realistic geometries. Two staggered grid explicit FD schemes which show promise for this purpose are assessed: the Lebedev FD scheme and the rotated staggered grid (RSG) FD scheme. Algorithmic points which provide challenges for complex geometries are addressed, in particular handling of traction free surfaces and bi-material interfaces present at lamina boundaries. Code execution time estimates are performed as well to guide feasible domain sizes relative to algorithm choice and available hardware. Three test cases are simulated: a delaminated plate, a cylinder, and a triclinic lamina. These tests demonstrate that the Lebedev FD scheme needs additional work to handle inter-laminar interfaces and traction free boundaries in the presence of stair-stepping approximations. In contrast, the simple structure of the RSG unit cell makes it more straightforward to construct a 3D simulation technique for curved composite laminates.

INTRODUCTION

The use of composites for structural and non-structural components continues to expand in the aerospace field. While composite materials are highly beneficial in aerospace applications, since they enable lightweight components/vehicles, they also bring unique challenges to the inspection of those components/vehicles. The damage types existing in carbon fiber reinforced polymer (CFRP) composites, typically used for aerospace applications, differ greatly from metallic materials. Defects that can occur in CFRP composites include delaminations, porosity, foreign object debris (FOD), matrix cracking, and fiber breakage [1]. Currently, ultrasound is one of the most widely used nondestructive evaluation (NDE) techniques for composite aerospace structures. However, composites pose inspection challenges for ultrasonic methods, particularly for complex geometries.

CFRP composites commonly are made of unidirectional prepreg layers rotated to different angles. For flat laminates, the resulting stiffness matrix can correspond to the case of monoclinic anisotropy. For complex geometry composites, additional material rotations (e.g., to follow the curvature of a hat stiffener), can result in triclinic anisotropy. The direction of ultrasonic energy propagation is affected by this anisotropy and can lead to the waves being guided in unexpected directions [2]. Such behavior makes it difficult to use experimental methods to optimize inspection of complex geometry composite parts. Additionally, the presence in composites of both anisotropy and complex damage states significantly impacts ultrasonic wave propagation, leading to NDE signals that are difficult to accurately interpret. Ultrasound simulation can aid in solving these two challenges by providing insight into the complicated wave propagation behavior in composites.

The validation, application, and assessment of ultrasound simulation methods/tools for composites, and specifically for complex geometry composites, is an area that currently has limited published work in the literature. Some examples of recent work for complex geometry composites includes a 2015 study by Reverdy et al. in which they apply a hybrid semi-analytical – finite difference (FD) method to curved composites [3]. In 2018, Panda and

colleagues published a study using finite element method (FEM) to simulate guided ultrasonic wave propagation in stiffened composites panels [4]. While there are a few examples of ultrasound simulation based studies for complex geometry composite simulations, the literature is lacking in benchmark and validation studies that enable a clear assessment the capabilities, limitations, and computational requirements of ultrasonic simulation tools (including commercial tools) for this application.

This paper discusses efforts to expand FD simulation techniques for use in 3D complex geometry CFRP composites. One benefit to FD approaches is that they can result in equations and associated computational code that are straightforward to derive and implement. Since the resulting equations herein form an explicit scheme, it becomes straightforward to parallelize efficiently on multi-core, many-core, or cluster computing resources. The FD approaches investigated in this work are the Lebedev and Rotated Staggered Grid (RSG) methods [5-7]. These two methods use staggered-grid FD techniques, however, they differ in the layout of variables on the computational and material grids. The Lebedev grid has been shown to need fewer grid cells to produce the same accuracy results, resulting in faster simulations and lower memory requirements. In contrast, the RSG is more straightforward in its handling of material interfaces and traction free boundaries. Both methods are widely used in the field of geophysics and there is limited work in the literature on applying them to ultrasound propagation in composites [8]. In this paper, FD simulation using Lebedev and RSG schemes are performed for simulating cases which challenge some of the aspects of moving towards complex geometry CFRP composites. The simulation codes for each FD scheme were developed using C++ and message-passing-interface (MPI) for parallelization.

The most pertinent challenges are employing a heterogeneous FD scheme to handle material interfaces, and implementing a traction free boundary formulation which is numerically stable for triclinic media. The following test cases are assessed: a flat delaminated plate (for comparison to a benchmark in the literature), a curved composite cylinder, and a plate case with triclinic anisotropy (to test the traction free boundary implementation) [9].

These topics are discussed in the following sections of this paper:

- An overview of Lebedev and RSG FD schemes, focusing on implementation details most pertinent to complex geometry composites
- Assessment of the delaminated plate, composite cylinder, and triclinic plate test cases
- A Lebedev code execution time study to compare algorithm performance and provide guidance on feasible simulation domain sizes

3D ELASTODYNAMIC FINITE DIFFERENCE FORMULATION

The formulation of the FD numerical schemes used in this work stem from the stress-velocity elastodynamic equations. In Cartesian coordinates these are

$$\begin{aligned} \rho \frac{\partial v_i}{\partial t} &= \frac{\partial \sigma_{ij}}{\partial x_j} + f_i^v \\ \frac{\partial \sigma_{ij}}{\partial t} &= c_{ijkl} \frac{\partial v_k}{\partial x_l} + f_i^\sigma \end{aligned} \tag{1}$$

where ρ is the mass density, c_{ijkl} are components of the stiffness tensor, v_i are components of the velocity vector, and σ_{ij} are components of the stress tensor. f_i^v and f_i^σ represent the components of the force source vector and the moment rate tensor, respectively [10].

Partial derivatives in space and time are then substituted with central difference approximations

$$\begin{aligned} D_{x_1}[f]_{ijk}^n &= \frac{f_{(i+1)jk}^n - f_{(i-1)jk}^n}{\Delta x_1} \\ D_t[f]_{ijk}^n &= \frac{f_{ijk}^{n+1/2} - f_{ijk}^{n-1/2}}{\Delta t} \end{aligned} \tag{2}$$

where D is the 2nd order central difference operator, Δx_1 is the cell size along the x_1-direction, and Δt the time step between steps n and $n+1$. Similar operators are used for the x_2 and x_3 directions. Subsequent rearrangement yields an explicit 'leapfrog' time-stepping scheme where for each subsequent time step, velocities are calculated from neighboring stress values, and vice versa. That is, the stress and velocity calculations proceed in half-time-step increments. The works of Lisitsa [5] and Saegner [6, 7] provide the requisite equations. Some algebraic manipulation

is still necessary to arrive at computationally implementable equations. Conceptually, the resulting equations are similar to the leapfrog scheme in the finite integration technique (EFIT) [11].

The requirement of velocities only to access neighboring stresses (and vice versa) provides a natural motivation for the use of what are termed 'staggered grid' FD schemes. In these types of schemes, simulation domains are constructed from repeating subunits of grid cells. Within these cells, a given spatial location contains some, but not all types of state variables (e.g. stresses or velocities). Fig. 1 shows the two types of grid cells (Lebedev and RSG) used in this work. Both are staggered grid schemes where either all three velocity or all six unique stress components are specified at a given point. This has the benefit that even for generally anisotropic media, no interpolation of state variables is necessary (this is not always the case, as in the case of EFIT). Storage or reference to 21 stiffness matrix components and density is done once at the center of each cell, and values are interpolated as necessary. In this work, grid cells are arranged in a Cartesian coordinate system, requiring stair-stepping approximations for inter-laminar interfaces and traction free boundaries. Although in principle, these grid schemes are amenable to curved implementations [12], further work would be needed to extend to 3D geometries a monoclinic or triclinic formulation.

FIGURE 1. Distribution of stress and velocity values for (a) Lebedev and (b) Rotated staggered grid unit cells

Material Interface Implementation

The choice of grid scheme naturally affects memory utilization due to differing number of state variables per grid cell. A detailed analysis can be found in the work of Lisitsa [5]. In short, Lebedev has higher memory utilization per grid cell, but due to a lower numerical dispersive error, requires fewer grid cells (and less memory) for a given simulation. Less immediately apparent, but equally important is the effect on the choice of algorithm for handling traction free boundaries and material interfaces. In our experience, these considerations are highly challenging in developing and implementing a FD scheme.

Material interfaces in FD analysis are typically handled using what is termed a heterogeneous FD scheme. Rather than explicitly imposing interface conditions, a set of effective material properties are found which identically satisfy conservation laws at the interface. This allows the same FD equations to be applied over the entire domain, greatly simplifying the implementation of a scheme and aiding in computational efficiency (e.g. by eliminating branching).

Momentum conservation at the interface is enforced by requiring the equivalence of normal stresses and transverse strains (or displacements) on either side. This was performed by Schoenberg and Muir [13], who showed that this technique satisfies transmission and reflection coefficients in the far-field. The effective stiffness matrix calculation requires a planar surface (or curved surface with a planar approximation [14]), and causes difficulties at corners and edges. Handling density is more straightforward, as a simple arithmetic averaging of the density is sufficient.

As an approximation to a momentum-conserving approach, Moczo [15, 16] prescribed using harmonic averaging of individual stiffness matrix values across the interface as an approximation to Schoenberg's approach. This has the advantage that it lifts requirement that the interface is planar. It also avoids increasing the number of elastic constants at the interface (although this is not a concern in a triclinic FD formulation). The downside is that approximation approaches such as this have been shown to miss qualitative features of wave propagation [14]; additionally, the harmonic average is not defined for negative numbers, which are admissible in triclinic material systems such as rotated CFRP. Although generally not recommended, arithmetic averaging of individual stiffness matrix coefficients has been used in the literature. This approach lacks the theoretical rigor or harmonic averaging or Schoenberg calculus, and has been proposed to result in a 1st order of approximation (as opposed to 2nd order for these other schemes) [17].

In terms of applicability to Lebedev and RSG FD schemes, the important note is that interface-effective elastic coefficients need to be calculated at the boundaries of a grid cell. For locations with velocity calculations, only density needs to be provided; for locations with stress calculations, only stiffness matrix components need to be provided. This presents some challenges for inter-laminar stair-stepping approximations in the Lebedev method (as in a curved interface between two lamina). Since the Lebedev grid cell has stresses at the edges, a stair-step over a curving lamina violates the Schoenberg calculus planar interface assumption, leaving an open question for how to calculate effective stiffness coefficients at edges. For RSG, only velocities are present at the edges of a grid cell, meaning that in RSG a simple arithmetic averaging of density is sufficient for a heterogeneous interface scheme, imposing no restrictions on applicable geometry. In this work, arithmetic averaging of densities at grid cell interfaces was used for both Lebedev and RSG schemes. For the Lebedev scheme, cases involving inter-laminar stair stepping were avoided in this work, and the Schoenberg calculus approach was used for planar inter-laminar interfaces.

We performed preliminary testing of heterogeneous interface approaches using the Lebedev scheme for an 18.0 mm x 18.0 mm x 21.6 mm bulk material region containing a monoclinic-triclinic bi-material interface (Fig. 2a). The model had a top IM7-8552 layer rotated by 30° about the z-axis and a bottom material layer rotated by 30° about the z-axis, followed by a 45° rotation about the y-axis). A 300 kHz 3-count Hann windowed point source tone burst was excited on the monoclinic side of the interface. The time step and cell size were 2.98 ns and 60 µm, respectively.

Employing an arithmetic-averaging material interface approach caused numerical instability at the interface. The use of harmonic averaging was not attempted, as there was no straightforward means to handle the negative C_{ij} values for the triclinic media. Use of the Schoenberg approach produced numerically stable results, both upon initial contact with the interface (Fig. 2b), as well as where the traction free boundary met the interface. Numerical comparisons between the Schoenberg approach with arithmetic and harmonic averaging showed significant discrepancies in C_{ij} values, with percent differences in the tens of percent for harmonic averaging (when applicable), and in the tens to hundreds of percent for arithmetic averaging. Since the Schoenberg averaging is what is guaranteed to produce accurate transmission and reflection in the far field, discrepancies of this order of magnitude from this value may significantly fail to appropriately treat boundary conditions thus, care must be taken. Even though approximate heterogeneous interface schemes converge, they may represent the 'wrong interface'. Due to this, it is recommended to use a conservation-based scheme whenever possible.

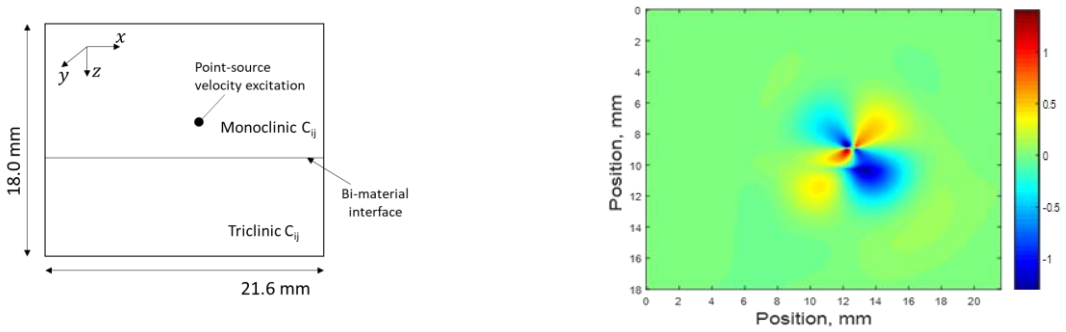

(a) (b)

FIGURE 2. Lebedev FD simulation stability upon interaction with a monoclinic-triclinic interface. (a) Sketch of model setup, and (b) v_x velocity wavefield at 4.46 µs (after interaction with the monoclinic-triclinic interface

Traction Free Boundary Implementation

Several approaches have been proposed in the literature for implementing traction free boundaries. The challenge in implementing a traction free boundary condition is that a naïve implementation of central differences at an interface require stress or velocity values from ostensibly nonexistent "vacuum" cells on the other side of the interface. A number of approaches have been proposed in the literature: e.g. traction imaging, vacuum formalisms, or use of backward-differences at boundaries. Part of the influence of the grid scheme is in which types of state variables (stress or velocity) are present at cell interfaces. This dictates whether stresses, velocities, or both need to be explicitly handled for traction free boundaries. Whether those state variables are located at faces, edges, or corners also influences the formulation.

In the Lebedev scheme, traction free boundaries require more careful attention, as both stress and velocity values are present at the outer boundaries of a grid cell where they can interact with a traction free surface. For stress equations, we followed the approach of Quintanilla [8]. Manipulation via Hooke's law at stress free surfaces allow a closed-form calculation of normal strain rate (which require vacuum values) in terms of tangential strain rate (which are amenable to calculation). Similar arguments hold for stress free edges when stair-stepping over a curved surface. This approach still left open the question of how to handle velocity calculations. A traction imaging approach was chosen [18, 19], such that stress values in vacuum are set to the negative of stress values in the solid. This approach implicitly prescribes zero stress at the interface while maintaining smoothness required for the spatial central difference operators.

The RSG traction free surface contains only velocities at cell interfaces, making traction free boundary implementation more straightforward. It is highly amenable to a vacuum formalism; the solid surface is padded with a single layer of vacuum cells. These cells are prescribed $C_{ij} = 0_{ij}$ and a very small density, e.g. $\rho = 10^{-12}$. For voids at a solid-vacuum interface, a new density is calculated via arithmetic averaging of the density of the eight adjacent cells. This is essentially handling traction free boundaries as a heterogeneous scheme [6, 13], treating the traction free boundary as a material interface between the solid and a zero-stress medium. In this method, the traction-free conditions are not explicitly imposed, but are instead encoded in the density calculations. There are no limitations on prescribed geometry, so this is applicable to faces, edges, and corners.

SIMULATION TEST CASES

Three simulation test cases were run using both Lebedev and RSG schemes. A delaminated plate case was run, following the works of Tian et al. [20] to give a comparison to experimental wave-damage interaction results. A verification was done on a curving CFRP cylinder geometry with the fiber-direction wrapping circumferentially. This was done to address stability and internal model consistency, particularly for stair-stepping approximations over free surface edges. Finally, a triclinic plate model was assessed. This model was found by Quintanilla and Leckey [8] to produce numerical instability in the elastodynamic finite integration technique (EFIT), but was stable for the Lebedev scheme. Therefore, the emphasis was on stability for the RSG scheme.

Delaminated Plate Validation

A simulation was performed to match an experimental laser Doppler vibrometry benchmark performed in the work of Tian et al. [20]. The plate was 90.0 x 60.0 x 0.8554 mm, consisting of eight plies of IM7-8552 in a $[90_2/0_2]_S$ layup, (Fig. 3). Material properties are given in Table 1. A 20.0 mm x 20.0 mm delamination was placed into the model by replacing the very top cells of the 3rd ply with vacuum cells. A 7.0 mm PZT transducer was simulated with a vertical v_z excitation of a 300 kHz 3-count Hanning windowed sine wave. The vertical excitation is an approximation to provide an input which excites S0 and A0 Lamb wave modes. An in-plane radial excitation about the lateral edges of the transducer region can be used to represent a pin-force model to better approximate a bonded transducer [20, 21].

The time step was set to 1.67 ns and the cell size was set to 35.6 µm, corresponding to three cells per lamina. It was found that two cells per lamina was sufficient for wavenumber convergence in the undamaged region. However, the wavelength reduction and the reduced thickness above the delamination necessitated the additional discretization.

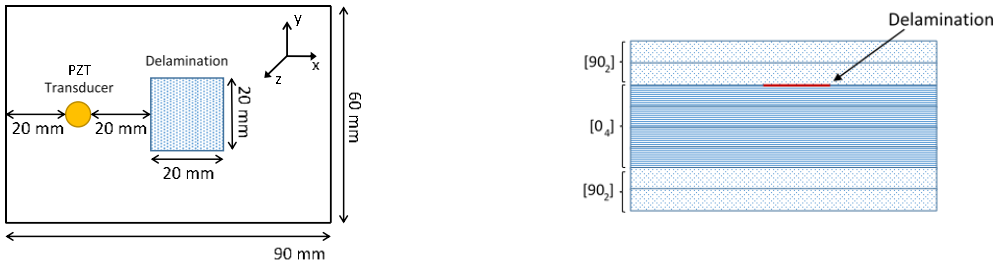

(a) (b)

FIGURE 3. Configuration of the delaminated plate test case. (a) Plate top with transducer and damage location, and (b) cross-sectional view showing the layup and depth of the delamination

Fig. 4 shows a v_z (out-of-plane velocity) wavefield of the top cell of the plate for both Lebedev and RSG schemes. Both simulations plots show characteristic features which were observed in the initial experimental-FD benchmark.

TABLE 1: Elastic properties for IM7/8552 CFRP, with fibers oriented in the 1-direction

ρ, kg/m^3	E_1, GPa	E_2, GPa	E_3, GPa	G_{12}, GPa	G_{13}, GPa	G_{23}, GPa	v_{12}	v_{13}	v_{23}
1570	171.4	9.08	9.08	5.29	5.29	2.80	0.32	0.32	0.5

'Pristine' S0 and A0 quasi-Lamb wave modes propagated through the undamaged region, and 'damaged' S0 and A0 wave modes propagated in the region above the delamination. Expected propagation characteristics were also observed in the simulations such as reflection and mode conversion upon initial wave interaction with the delamination, as well as resonance effects in the region above the delamination.

A frequency-wavenumber analysis was performed (Fig. 5) along a line covering from the edge of the transducer to the far edge of the delamination, from 0-33.4 μs to obtain the forward-propagating components of the wave. Both 'pristine' and 'damaged' A0 wave modes are observed, matching direct solution of the A0 wave mode from DISPERSE software [22] for both the 8-layer laminate and for the 2 layers immediately above the delaminated region. Only the A0 wave modes can be seen in the v_z wavefield, as the S0 mode (which has a small component of out-of-plane velocity) is overshadowed by the larger amplitude 'pristine' and 'damaged' A0 modes.

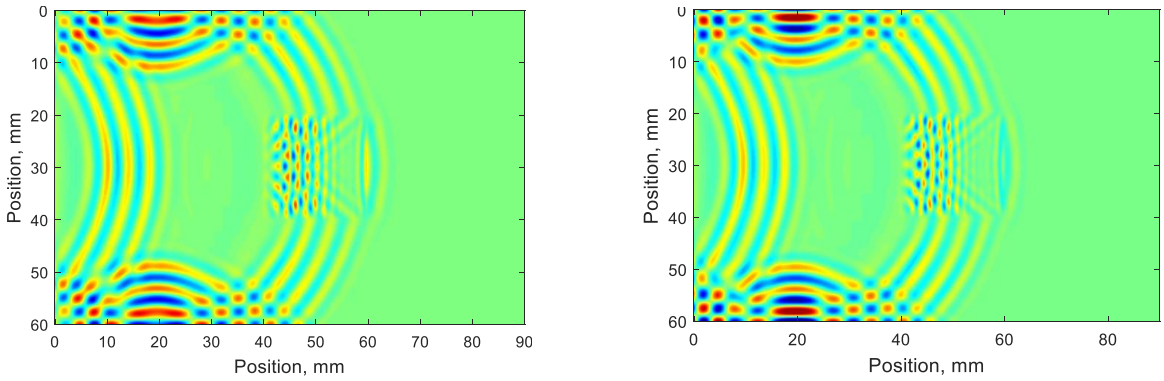

(a) (b)

FIGURE 4. Delaminated plate out-of-plane (v_z) velocity wavefield at 27.85 μs for (a) Lebedev and (b) RSG grids

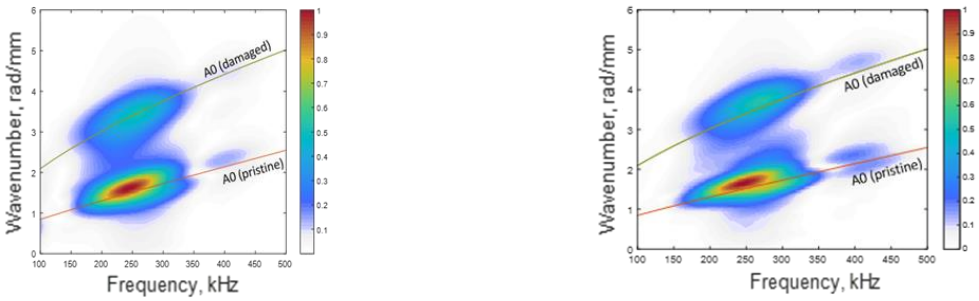

(a) (b)

FIGURE 5. Normalized frequency-wavenumber dispersion curves for (a) Lebedev and (b) RSG simulations

Although the Lebedev and RSG simulations show the same general overall behavior, the simulations are not fully equivalent in the vicinity of traction free boundaries, as shown by wavefields at the same time frame in Fig. 4a,b**.** For example, Lebedev is showing a higher curvature of wave fronts upon reflection from lateral plate sides, and a higher amplitude at the far-side of the delamination. In contrast, propagating prior to reflection appears consistent between the Lebedev and RSG schemes. Our interpretation for the cause is due to the phenomenon of artifact modes which

can propagate through a Lebedev grid [23]. In this phenomenon, the grid cell contains additional non-physical wave modes not specified by the elastodynamic equations. For bulk wave propagation, these modes can be identically forced to zero via a mapping procedure. This is done by specifying forces at a cell centers, then redistributing via weighted-average to each cell's constituent grid points. This is followed by averaging state variables back to cell centers for output to obtain the physically admissible results [5]. However, it was found that the Lebedev simulation permitted conversion from elastic modes back into artifact modes at edges, e.g. edges of both the plate and the delamination. This could be observed by an even-odd decouple which would emerge in the nodal data prior to the averaging velocities back to cell centers. This phenomenon was not present upon reflection from planar surfaces, but was observed upon reflection from the twelve edges of the plate and the twelve edges of the delamination.

Curving Geometry

Circumferential propagation around a cylinder was used to test both fiber orientation functionality and the code's stability for curving interfaces. In the future, we plan to move towards quantitative comparisons with a curving geometry such as comparison of circumferential dispersion curves. At present, this case is being used for model verification only, in terms of testing for stability and internal consistency based on expected features for guided waves.

(a) (b)

FIGURE 6. (a) Dimensions of a cylinder verification model, with (b) fiber oriented circumferentially around the cylinder

The cylinder geometry has a 20 mm inner diameter, 1 mm wall thickness, and 40 mm length (Fig. 6a). The local fiber direction was oriented circumferentially around the cylinder (Fig. 6b); this fiber direction was used as an input to the simulation code, which used it to construct the rotated stiffness matrix for each cell. The material is comprised of IM7-8552 with material properties in Table 1 (with the exception that $C_{44} = (C_{22} - C_{23})/2$ was instead calculated for transversely isotropic symmetry). The cell size was set at 62.5 µm, providing a minimum of 16 cells per wall thickness throughout, and the time step was set to 2.93 ns. The top outer surface of the cylinder was excited with a point source 300 kHz, 3-count Hann windowed tone burst.

A series of three intuitive verifications on circumferential wave propagation was sufficient for this analysis:

1. Propagation clockwise and counterclockwise should be equivalent
2. The normal of the wave fronts should remain oriented in the circumferential direction of the cylinder
3. The velocity field should remain continuous and resulting wavefield remain stable

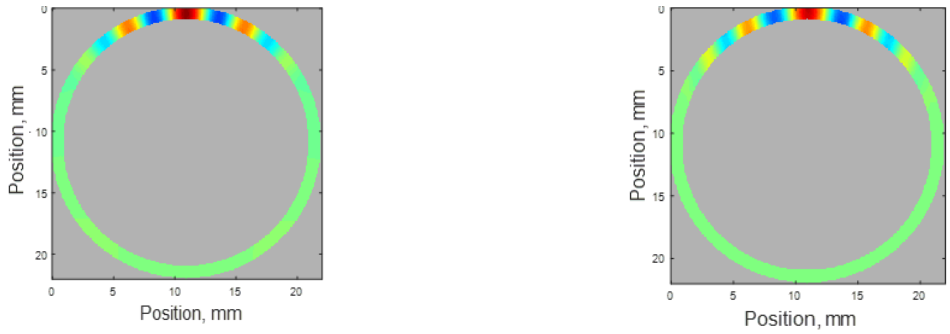

(a) (b)

FIGURE 7. Velocity v_2 wavefield at 7.32 µs showing circumferential propagation for (a) Lebedev and (b) RSG FD schemes

Wavefields from Lebedev and RSG simulations are shown in Fig. 7a,b. While not obvious in the plots, through direct velocity value comparisons, it was found for Lebedev that propagation clockwise and counterclockwise was not quite equivalent. In contrast, RSG was able to meet this criteria. For both models, the wave fronts remained oriented circumferentially around the cylinder, following both the fiber orientation and the cylindrical waveguide. It is interesting to note that for a coarser discretization, the wave fronts lagged behind the appropriate wave front rotation, a possible explanation being the influence of overly coarse stair-stepping approximations. Perhaps the most pertinent and interesting note is the effect on stability. The RSG FD simulation exhibited no signs of mounting numerical error, discontinuity in wavefields, or instability. The Lebedev FD simulation, on the other hand, first started exhibiting discontinuities at edges. The magnitude of these discontinuities mounted until the simulation became numerically unstable. Just as in the delamination case, the source of error is believed to be due to mode conversion into numerical artifact modes at edges. There are a large number of edges present over the numerous cell 'stair-steps' used to approximate the curved surface. Repeat interaction with this large number of edges caused the errors (and eventual numerical instability) to mount faster than in flat laminate cases which have few edges.

Stability for Triclinic Media

One of the main motivations of the choice of Lebedev scheme was its stability for triclinic media, in particular upon interaction with traction free boundaries, as this was found to be one of the major drawbacks of EFIT for curved composites. Quintanilla [8] demonstrated stability using a Lebedev grid for a triclinic plate with traction free surface. Saegner [7] indicated that the RSG scheme is stable for triclinic media with traction free surfaces, but we have not found a test in the literature which confirms this. To this end, we simulated propagation in a triclinic plate for the RSG scheme to confirm stability.

A 60.0 x 60.0 x 1.08 mm flat triclinic lamina was simulated. The cell size was set at 60 μm, and the time step set to 2.98 ns. The material properties for IM7-8552 (Table 1) were used. To cause the lamina to be triclinic, the stiffness matrix was rotated first by 30 degrees about the global z-axis (the thickness-direction), followed by a rotation of 45 degrees about the global y-axis, resulting in a stiffness matrix with all non-zero elements. The excitation was given by a 3-count Hann windowed sine wave at 300 kHz excited in the z-direction, distributed over a 0.6 mm diameter at the top cell. Normalized v_z plots for the top cell are shown in Figure 8. These show the wavefield orienting along the new fiber direction. The waves are also stable following edge reflection, indicating overall stability for triclinic media.

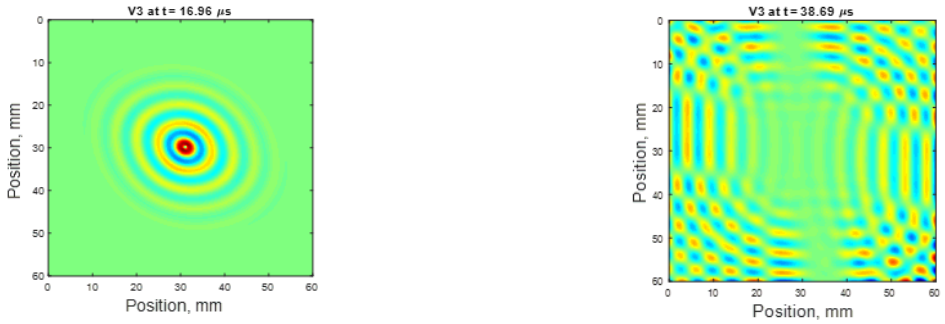

(a) (b)

FIGURE 8. RSG triclinic plate normalized v_z (a) prior to edge reflection at 16.96 μs and (b) remaining stable following lateral edge reflection at 38.69 μs

SIMULATION CODE EXECUTION TIME ASSESSMENT

Further development of the RSG elastodynamic simulation code will focus on further validation testing and optimization for improved execution time. As with all software optimization, hardware-awareness is required to achieve the most efficient use of the processing capabilities, and lower bound estimates on execution time are important to guide optimization. To this end, a similar FD code for isotropic EFIT has been developed at NASA Langley Research Center, optimized for the Intel Xeon Phi Knights Landing (KNL) manycore processor [24]. This isotropic EFIT was optimized using techniques which are also applicable to the Lebedev and RSG schemes.

The application of these FD algorithms are communication-bound, i.e. the execution time is limited by the rate at which data can be supplied to the processors. Because of this, the realized speed of the isotropic EFIT code can be used as a baseline to provide estimated execution time based on RSG and Lebedev data movement requirements.

The memory occupancy per grid cell is calculated using 32 bit floating point variables for elastic coefficients (21 C_{ij}'s and density), and 64 bit double precision floating point variables for the state variables. An upper bound for execution time, calculated in terms of time/(cell*time step) is obtained by dividing the memory occupancy by the MCDRAM bandwidth of 400 GB/s. Achievable execution time is then obtained by scaling the lower execution time bound based on the performance of the optimized EFIT code, which took 3.25 times longer to run than the optimal execution time. The optimized isotropic EFIT code achieved an execution time of 0.78 ns / (cell * time step). Expecting similar inefficiencies in implementation, estimated execution times for Lebedev and RSG codes are, respectively, 3.77 and 2.02 ns / (cell * time step). See Table 2 for a breakdown of memory occupancy and code execution time estimates.

An even more aggressive optimization would be to store the 9 constants for orthotropic material once, and for every cell store the three rotation angles required to construct the rotated stiffness matrix. Following this approach, the rotated stiffness matrix would need to be constructed for each cell at every time step. As long as the code continues to be bandwidth-bound (e.g. the net effect of evaluating trigonometric functions doesn't excessively increase compute time), the reduced grid cell memory occupancy reduces execution time. Continuing with the assumption that the isotropic EFIT works as a timing surrogate, estimated achievable execution times for Lebedev and RSG are, respectively, 2.47 and 0.72 ns / (cell * time step). These optimizations are shown in Table 2 marked as '3 angles'.

To translate performance estimations into more intuitive terms, consider a nominal case of a 180 mm x 180 mm x 1.0 mm plate, with a total simulation time of 118.8 μs (3000 x 3000 x 20 cells for 40,000 time steps). Single node total execution time and 4-node execution time with a perfect strong scaling approximation are shown in Table 3. The longest 4-node execution time is the Lebedev scheme storing 21-$C_{ij}'s$ for each cell, at 1.9 hours. An aggressive optimization of RSG storing only the 3-rotation angles cuts this down to 0.36 hours. Although, this would require optimization not only of the stencil calculations, but the stiffness matrix rotation. Therefore, this should only be undertaken if faster execution times are worth the additional time to optimize a larger section of code.

TABLE 2: Estimated simulation execution time for Lebedev and RSG using optimized isotropic EFIT code as a reference. *Normalized execution time estimates are calculated as time per (cell*time step)

	Lebedev (21 C_{ij}'s)	Lebedev (3 Angles)	RSG (21 C_{ij}'s)	RSG (3 Angles)	Isotropic EFIT (2 Lamé parameters)
State Variables per Cell	36	36	9	9	9
Elastic parameters per cell	22	4	22	4	3
Data per Cell, Bytes	464	304	248	88	96
Normalized Optimum time, ns*	1.16	0.76	0.62	0.22	0.24
Normalized Achievable time, ns*	3.77	2.47	2.02	0.72	0.78

TABLE 3. Execution time estimations for a 200 kHz excitation on a 180 mm x 180 mm x 1 mm IM7-8552 plate for 118.8 μs (3000 x 3000 x 20 cell for 40,000 time steps). 4-node cluster time assumes perfect strong scaling

	Lebedev (21 C_{ij}'s)	Lebedev (3 Angles)	RSG (21 C_{ij}'s)	RSG (3 Angles)
Single-node execution time, hours	7.5	4.9	4.0	1.2
Four-node execution time, hours	1.9	1.4	1.0	0.36

CONCLUSIONS AND FUTURE WORK

This work addressed an ongoing process of developing and testing a framework for FD simulation of 3D curving laminated composites. Two FD schemes were considered: Lebedev and RSG. It was found that Lebedev, as formulated, provides two major impediments to its employment in curving laminates. This presents itself in terms of 1) mode conversion to artifact modes at traction free boundaries with stair-stepping approximations, and 2) the

inability to apply a conservation-based scheme at stair-stepping bi-material interfaces. In contrast, RSG did not present these restrictions. Comparison at early time steps in a delaminated plate model and a cylinder model showed the two methods are similar, particularly early in the simulation; however, numerical errors mounted for Lebedev when repeat interactions with edges occurred, precluding its effective use. This is not to say that Lebedev method is ineffective, but rather needs additional enhancements in its formulation. Since a triclinic simulation using EFIT is unstable at lateral plate edges, a triclinic plate test was run for RSG, showing that it was stable for triclinic media with traction free boundary conditions. Prior work showed that the Lebedev scheme is also stable for triclinic media.

This work focused largely on the 'compute kernel' portion of a simulation workflow. However, in practice, much of the labor involved in simulation of complex geometries is dedicated to domain construction tasks. This is particularly true for voxelization and the generation of fiber orientation data for complex geometries. Going forward, we are continuing this work by automating portions of the complex geometry framework. This includes developing a well-defined application-program interface that can interact with existing open-source codes (such for efficient voxelization [25]), as well as developing/adapting tools to help with obtaining fiber orientation data. In parallel, we are also in the process of developing an optimized compute kernel for RSG, looking to achieve simulation times seen in the execution time assessment, or higher with performance portability to higher bandwidth systems.

ACKNOWLEDGMENTS

Dr. Elizabeth Gregory, Dr. Francisco Quintanilla, and Peter Juarez are gratefully acknowledged for their contributions to this work in the form of scientific discussion and advisement.

REFERENCES

[1] I. Daniel, O. Ishai, *Engineering Mechanics of Composite Materials* (Oxford University Press, New York, 1994).
[2] J. Rose, *Ultrasonic waves in solid media* (Cambridge University Press, Cambridge, 2000): 1807-1808.
[3] F. Reverdy, S. Mahaut, N. Dominguez, P. Dubois, in AIP Conference Proceedings (AIP, 2015) Vol. 1650 pp. 1047–55.
[4] R. S. Panda, P. Rajagopal, K. Balasubramaniam, Compos Struct 247-260, 206 (2018).
[5] Lisitsa V, Vishnevskiy D. Lebedev scheme for the numerical simulation of wave propagation in 3D anisotropic elasticity. Geophys Prospect. 2010;58(4):619–35.
[6] E. Saenger, N. Gold, S. Shapiro, Wave Motion 77-92, 31 (2000).
[7] E. Saenger, T. Bohlen, Geophysics 583-591, 69 (2004).
[8] F. Quintanilla, C. Leckey, Ultrasonics 28-40, 86 (2018).
[9] C. Leckey, K. Wheeler, V. Hafiychuk, H. Hafiychuk, D. Timuçin, Ultrasonics 187-200, 84 (2018).
[10] J. Virieux, H. Calandra, R- É Plessix, Geophys Prospect. 794-813, 59 (2011).
[11] C. Leckey, M. Rogge, C. Miller, M. Hinders, Ultrasonics 193-207, 52 (2012).
[12] C. Pérez Solano, D. Donno, H. Chauris, Comput. Geosci. 245-264, 20 (2016).
[13] M. Schoenberg, F. Muir, Geophysics 581-589, 54 (1989).
[14] F. Muir, J. Dellinger, J. Etgen, D. Nichols, Geophysics 1189-1193, 57 (1992).
[15] P. Moczo, J. Kristek, V. Vavryčuk, R. Archuleta, L. Halada, Bull. Seismol. Soc. Am. 3042-3066, 92 (2002).
[16] P. Moczo, J. Robertsson, L. Eisner Adv Geophys. 421-516, 48 (2007).
[17] V. Lisitsa, O. Podgornova, V. Tcheverda, Comput Geosci. 769-778, 14 (2010).
[18] A. Levander, Geophysics 1425-1436, 53 (1988).
[19] R. Graves, Bull. Seismol. Soc. Am. 1091-1106, 86 (1996).
[20] Z. Tian, L. Yu, C. Leckey, Journal of Intelligent Material Systems and Structures 1723-1738, 26 (2015).
[21] V. Giurgiutiu, *Structural Health Monitoring with Piezoelectric Wafer Active Sensors, 2nd ed.* (Elsevier, Oxford, 2014).
[22] B. Pavalakovic, M. Lowe, *DISPERSE: A System for Generating Dispersion Curves, User's Manual* (Imperial College of London, 2000).
[23] V. Lisitsa, D. Vishnevsky, Numer. Anal. Appl. 125-135, 4 (2011).
[24] W. Schneck III, E. Gregory, C. Leckey, J. Comput. Phys. 550-562, 374(2018).
[25] G. Young, A. Krishnamurthy Comput Graph. 11-24, 75 (2018).